

## CONSTRAINTS ON NEUTRON STAR PROPERTIES FROM X-RAY OBSERVATIONS OF MILLISECOND PULSARS

SLAVKO BOGDANOV, GEORGE B. RYBICKI, AND JONATHAN E. GRINDLAY  
sbogdanov@cfa.harvard.edu, grybicki@cfa.harvard.edu, jgrindlay@cfa.harvard.edu  
Harvard-Smithsonian Center for Astrophysics, 60 Garden Street, Cambridge, MA 02138  
*Draft version August 18, 2018*

### ABSTRACT

We present a model of thermal X-ray emission from hot spots on the surface of a rotating compact star with an unmagnetized light-element atmosphere. An application to *ROSAT*, *Chandra*, and *XMM-Newton* X-ray observations of the nearest known rotation-powered millisecond pulsar (MSP) PSR J0437–4715 reveals that the thermal emission from this pulsar is fully consistent with such a model, enabling constraints on important properties of the underlying neutron star. We confirm that the observed thermal X-ray pulsations from J0437–4715 are incompatible with blackbody emission and require the presence of an optically thick, light element (most likely hydrogen) atmosphere on the neutron star surface. The morphology of the X-ray pulse profile is consistent with a global dipole configuration of the pulsar magnetic field but suggests an off-center magnetic axis, with a displacement of 0.8 – 3 km from the stellar center. For an assumed mass of 1.4  $M_{\odot}$ , the model restricts the allowed stellar radii to  $R = 6.8 - 13.8$  km (90% confidence) and  $R > 6.7$  km (99.9% confidence), which is consistent with standard NS equations of state and rules out an ultracompact star smaller than its photon sphere. Deeper spectroscopic and timing observations of this and other nearby radio MSPs with current and future X-ray facilities (*Constellation-X* and *XEUS*) can provide further insight into the fundamental properties of neutron stars.

*Subject headings:* pulsars: general — pulsars: individual (PSR J0437–4715) — stars: neutron — X-rays: stars — gravitation — relativity

### 1. INTRODUCTION

After four decades of considerable observational and theoretical investigation of neutron stars (NSs), very little is known about several key properties of these objects. In particular, there is very limited information concerning their magnetic field configuration, surface properties, and structure and composition of their interiors. Thermal radiation from the physical surface of a NS can potentially serve as a useful tool in the study of these properties. For instance, a measure of the surface temperature can provide insight into the structure of the stellar interior through comparison with theoretical NS cooling models (see, e.g., Page 1998, and references therein), although it relies on an accurate age determination which is not easily measurable for most systems. In addition, mapping the temperature variations across the surface may be used to deduce the topology of the surface magnetic field of strongly magnetized NSs. Surface emission can also be used to infer the compactness of the star through measurement of the gravitational redshift  $z_g$ . In practice, this endeavor has proven to be quite difficult due to the absence of spectral lines (see, however, Cottam et al. 2006). For a NS radiating from the entire surface, the gravitational redshift can be obtained by determining the effective emission radius,  $R_{\text{eff}}$ . However, this method assumes that the inferred radius is exactly equal to the radius at infinity,  $R^{\infty} = (1 + z_g)R$ , of the star. As such it is subject to uncertainties in the emission properties of and exact temperature distribution across the stellar surface, as well as the distance to the source.

A promising approach is to study systems in which the thermal radiation is confined to a very small fraction of

the stellar surface ( $R_{\text{eff}} \ll R$ ). Such emission geometry is observed in rotation- and accretion-powered millisecond pulsars (MSPs) as well as old normal pulsars. In these objects, modeling the spectrum and rotation-induced variations of the observed flux can provide a measure of the compactness of the NS (see Pavlov & Zavlin 1997; Zavlin & Pavlov 1998). Moreover, the hot spots on the surface are believed to coincide with the polar caps, where the magnetic field is anchored to the NS surface, thus, allowing one to determine the geometry of the NS magnetic field. In addition, the modulation of the observed flux caused by the changing projection of the emission area permits study of the radiation pattern of the emergent intensity (isotropic versus anisotropic).

Herein, we present model spectra and lightcurves of compact stars with hot spots covered by a hydrogen atmosphere. An application of our model to archival *ROSAT*, *Chandra*, and *XMM-Newton* observations of the radio MSP J0437–0437 permits us to gain valuable insight into several fundamental NS parameters. This work represents an extension of similar studies by Pavlov & Zavlin (1997) and Zavlin & Pavlov (1998). The present paper is organized in the following manner. In §2 we outline the theoretical model, while in §3 we describe its practical application. We offer a discussion in §4 and give conclusions in §5.

### 2. THEORETICAL MODEL

Models of rotating compact stars with hot spots have been presented in a host of publications (e.g., Pechenick et al. 1983; Ftaclas et al. 1986; Riffert & Mészáros 1988; Miller & Lamb 1998; Braje et al. 2000; Beloborodov 2002;

Poutanen & Gierliński 2003; Viironen & Poutanen 2004; Cadeau et al. 2007). However, with some notable exceptions (e.g., Zavlin et al. 1995a; Pavlov & Zavlin 1997; Zane & Turolla 2006), these studies have assumed the idealized case of blackbody emission, i.e. an emergent intensity independent of angle. Here, we examine in-depth the observable properties of compact stars with light-element atmospheres and illustrate the key differences from blackbody emission. Below, we outline the basic formalism describing the system geometry and photon propagation.

### 2.1. Geometry

The basis of the model consists of a compact star of mass  $M$ , radius  $R$ , spin period  $P$ , and two antipodal hot spots<sup>1</sup> with  $R_{\text{eff}} \ll R$ . We designate the hot spot that approaches closer to the observer as the primary and define the closest approach as rotational phase zero ( $\phi = 0$ ). The magnetic axis is inclined at an angle  $\alpha$  with respect to the spin axis, while the spin axis is at an angle  $\zeta$  relative to the line of sight to a distant observer. The position of the primary hot spot on the NS surface is defined by the angle between the normal to the surface and the line of sight:

$$\cos \psi(t) = \sin \alpha \sin \zeta \cos \phi(t) + \cos \alpha \cos \zeta \quad (1)$$

An expression for the secondary hot spot is easily obtained by substituting  $\alpha \rightarrow \pi - \alpha$  and  $\phi \rightarrow \pi + \phi$ . Note that  $\alpha$  and  $\zeta$  are interchangeable as they figure in equation (1) in the same way.

In Schwarzschild geometry, due to the compact nature of the NS, the gravitational field has a profound effect on the photons as they propagate from the stellar surface to infinity. In particular, the energy of a photon is reduced by a factor of  $1 + z_g = (1 - R_S/R)^{-1/2}$ , where  $R_S = 2GM/c^2$ , as it escapes from the deep gravitational potential (see, e.g., Misner, Thorne, & Wheeler 1970). Furthermore, a photon emitted at an angle  $\theta > 0$  with respect to the local radial direction follows a curved trajectory and is observed at infinity at an angle  $\psi > \theta$ . The relation between these two angles is given by (Pechenick et al. 1983):

$$\psi = \int_R^\infty \frac{dr}{r^2} \left[ \frac{1}{b^2} - \frac{1}{r^2} \left( 1 - \frac{R_S}{r} \right) \right]^{-1/2} \quad (2)$$

where

$$b = \frac{R}{\sqrt{1 - R_S/R}} \sin \theta \quad (3)$$

is the impact parameter at infinity of a photon emitted from radius  $R$  at an angle  $\theta$ . In many practical situations, one can use a more convenient approximate relation between  $\psi$  and  $\theta$  (Zavlin et al. 1995a; Beloborodov 2002)

$$\cos \psi \approx \frac{\cos \theta - R_S/R}{1 - R_S/R} \quad (4)$$

which is valid for  $R > 2R_S$  and is remarkably accurate (fractional error of order a few percent). One interesting consequence of the bent photon trajectories is that most

of the NS surface is observable at any given time. In flat spacetime, the visibility condition is simply  $\cos \psi = \cos \theta > 0$ , while in Schwarzschild geometry a point on the neutron star surface is visible down to a critical angle  $\cos \psi_c$ , corresponding to  $b_{\text{max}} \equiv R^\infty = R/\sqrt{1 - R_S/R}$ , the apparent radius of the star.

### 2.2. Doppler Effect and Time Delays

For rotation- and accretion powered MSPs, the rapid motion of the NS surface induces an appreciable Doppler effect, parameterized through the familiar Doppler factor

$$\eta = \frac{1}{\gamma(1 - v/c \cos \xi)} \quad (5)$$

where  $\gamma = 1/\sqrt{1 - (v/c)^2}$ ,  $v = 2\pi R/P(1 - R_S/R)^{-1/2} \sin \alpha$  is the velocity of the hot spot as measured in the inertial frame of the hot spot, and  $\xi$  is the angle between the direction of the velocity vector and the line of sight. As shown by Poutanen & Gierliński (2003) and Viironen & Poutanen (2004), this angle can be expressed in terms of  $\theta$ ,  $\psi$ ,  $\alpha$ , and  $\phi$  as

$$\cos \xi = -\frac{\sin \theta}{\sin \psi} \sin \alpha \sin \phi \quad (6)$$

where the quantity  $\sin \theta/\sin \psi$  can be approximated by its asymptotic value for small angles  $(1 - R_S/R)^{1/2}$ .

We note that the assumption of a spherical Kerr metric does not lead to an appreciable difference in the shape of the lightcurves compared to the Schwarzschild case (as demonstrated by Cadeau et al. 2007). We also emphasize that for  $P \lesssim 3$  ms deviations from spherical symmetry such as rotation-induced oblateness becomes important. Cadeau et al. (2007) have found that in that regime neither the spherical Schwarzschild nor spherical Kerr metrics provide an accurate description of the properties of the rotating star. Therefore, the validity of our model is limited to spin periods greater than  $\sim 3$  ms.

Photons emitted from the far side of the NS relative to the observer, in addition to following a curved trajectory, have to travel a greater distance compared to a photon emitted radially. The resulting time lag of the photon as seen by a distant observer is given by the elliptical integral (Pechenick et al. 1983)

$$\Delta t(b) = \frac{1}{c} \int_R^\infty \frac{dr}{1 - R_S/R} \left\{ \left[ 1 - \frac{b^2}{r^2} \left( 1 - \frac{R_S}{r} \right) \right]^{-1/2} - 1 \right\} \quad (7)$$

This time delay translates into a phase lag ( $\Delta\phi$ ) of a photon

$$\Delta\phi = \frac{2\pi}{P} \Delta t \quad (8)$$

which yields the observed phase  $\phi_{\text{obs}} = \phi + \Delta\phi$  (Viironen & Poutanen 2004). For  $R/R_S \approx 2.5$ , the maximum  $\Delta t$ , corresponding to a photon with maximum impact parameter  $b_{\text{max}} = (1 + z_g)R$ , is of order  $60 \mu\text{s}$ , or  $\lesssim 6\%$  of the pulsar period for  $P > 1$  ms. Therefore, propagation time differences have a minor effect on the observed lightcurves even for the most rapidly rotating neutron stars. Nonetheless, this effect has been included in our model for completeness.

<sup>1</sup> In §3 we also consider the case when the hot spots are not antipodal.

The observed flux per unit frequency from each spot is given by

$$F(\nu) = I(\nu)d\Omega \quad (9)$$

where  $I(\nu)$  is the intensity of the radiation as measured at infinity and  $d\Omega$  is the apparent solid angle subtended by the hot spot. Transforming both quantities to the rest frame of the hot spot yields

$$F(\nu) = (1 - R_S/R)^{1/2} \eta^3 I'(\nu', \theta') \cos \theta' \frac{d \cos \theta}{d \cos \psi} \frac{dS'}{D^2} \quad (10)$$

where the primed quantities are measured in the NS surface rest frame (Poutanen & Gierliński 2003), with  $\cos \theta' = \eta \cos \theta$  and  $dS \cos \theta = dS' \cos \theta'$ .  $I'(\nu', \theta')$  is the emergent intensity,  $dS'$  is the emission area and  $D$  is the distance. The three Doppler factors arise from the transformation of the intensity. A fourth factor is obtained upon integration of equation (10) over a frequency interval since  $d\nu = (1 - R_S/R)^{1/2} \eta d\nu'$ . The total observed flux for a given rotational phase is found by relating  $\phi$  and  $\theta$  for each hot spot through  $\psi$  via equations (1) and (2), using the corresponding  $I'(\nu', \theta')$  in equation (10), and summing the flux from the two hot spots. Equation (10) allows one to generate a phase-integrated spectrum by simply integrating over the whole rotation period. It can also be used to construct an arbitrary emission region on the NS surface by considering multiple surface elements.

### 2.3. Atmosphere Model

To describe the emission properties of the stellar surface we use the hydrogen atmosphere model from McClintock et al. (2004) (see also Heinke et al. 2006)<sup>2</sup> having the following set of assumptions. The atmosphere is static, in radiative equilibrium, and composed purely of hydrogen. The scale heights in the atmosphere are much smaller than the NS radius so a plane-parallel approximation is valid. The star is weakly magnetized ( $B \ll 10^9$  G), meaning that the effects of the magnetic field on the opacity and equation of state of the atmosphere can be ignored (see e.g., Shibano et al. 1992; Zavlin et al. 1995b, for a treatment of magnetized atmospheres). The opacity within the atmosphere is due to thermal free-free absorption plus Thomson scattering in the unpolarized, isotropic approximation. For the temperatures of interest ( $\sim 10^6$  K) we expect complete ionization implying that bound-free and bound-bound transitions are unimportant. Finally, this model is valid for temperatures below  $T_{\text{eff}} \approx 3 \times 10^6$  K, where the effects of Comptonization within the atmosphere are negligible.

An important characteristic of light-element NS atmosphere models is that the peak emission occurs at higher energies than a blackbody (BB hereafter) for the same effective temperature (Romani 1987; Zavlin et al. 1996). Furthermore, the emission pattern of the atmosphere is inherently anisotropic with intensity decreasing as a function of angle with respect to the normal, resulting in a limb-darkening effect (cf Fig. 7 of Zavlin et al. 1996). This implies that although the emission spectrum of such an atmosphere is qualitatively similar to the case of a BB, the observed rotation-induced variation of the hot spot

<sup>2</sup> This model is virtually identical to that presented by Zavlin et al. (1996).

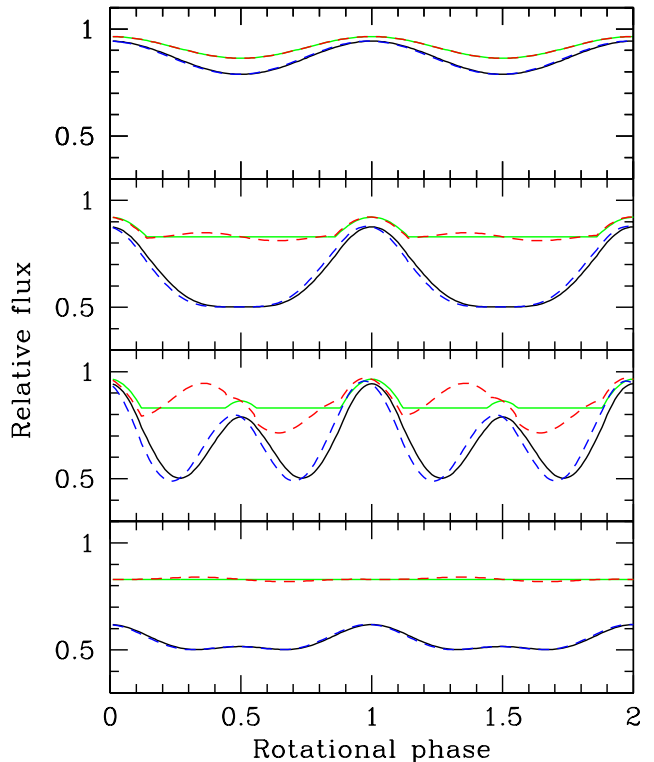


FIG. 1.— Representative model lightcurves for a rotating  $M = 1.4 M_{\odot}$ ,  $R = 10$  km NS with two point-like antipodal hot spots. The panels show classes I ( $\alpha = 10^{\circ}$ ,  $\zeta = 30^{\circ}$ ), II ( $\alpha = 30^{\circ}$ ,  $\zeta = 60^{\circ}$ ), III ( $\alpha = 60^{\circ}$ ,  $\zeta = 80^{\circ}$ ), and IV ( $\alpha = 20^{\circ}$ ,  $\zeta = 80^{\circ}$ ) as defined by Beloborodov (2002). The solid lines in each plot correspond to a hydrogen atmosphere (black) and blackbody emission (grey) with no Doppler effect included. The dashed lines show the effect of Doppler boosting and aberration for  $P = 4$  ms. All fluxes are normalized to the value for  $\alpha = \zeta = 0$ . Two rotational cycles are shown for clarity.

flux will be profoundly different. Figure 1 shows a sample of lightcurves, generated using equation (10) for a range of  $\alpha$  and  $\zeta$  for both BB and H atmosphere models, assuming  $M = 1.4 M_{\odot}$  and  $R = 10$  km. The most notable observable property of the atmosphere lightcurves is the substantially larger “depth” (i.e. pulsed fraction) relative to the BB case. Effectively, the limb darkening of the atmosphere acts to partially negate the effect of light bending, which tends to reduce the degree of modulation. Note, however, that even in the case of point-like hot spots, the modulations are still quite broad. In addition, it is not possible to achieve arbitrarily large pulsed fractions ( $\sim 100\%$ ) for any combination of  $\alpha$  and  $\zeta$ . These characteristics can be used to distinguish between thermal and non-thermal pulsed emission in cases where the spectral continuum alone does not provide sufficient information (see e.g. Chatterjee et al. 2007, for the case of PSR J0737–3039A). Limb darkening also significantly diminishes the effect of Doppler boosting on the shape of the pulse profile relative to the BB model, as evident in Figure 1. This is because, for a given hot spot, when the component of the velocity vector along the line of sight is largest (corresponding to a maximum Doppler boost) the hot spot provides a very small contribution to the total flux.

Unlike a BB, the pulsed fraction of the atmosphere emission is expected to vary depending on the choice of

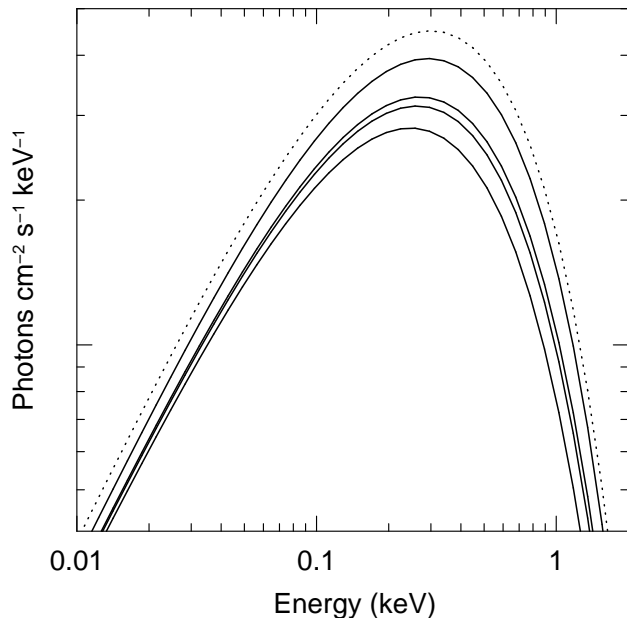


FIG. 2.— Phase-integrated synthetic H atmosphere hot spot emission spectra for  $M = 1.4 M_{\odot}$ ,  $R = 10$  km, and  $T_{\text{eff}} = 2 \times 10^6$  K. The solid lines correspond to classes I, III, II, and IV, from top to bottom, respectively, with values of  $\alpha$  and  $\zeta$  as in Figure 1. The dotted line is for a star with one hot spot always face-on ( $\alpha = \zeta = 0$ ). For all spectra the same arbitrary  $R_{\text{eff}}$  is assumed. Note the shifts in peak energy.

energy band due to the energy-dependent optical depth of the hydrogen layer (Zavlin et al. 1996). This marked difference between the atmosphere and BB lightcurves allows one to discriminate between the two emission models. For phase-resolved spectra of an atmosphere we expect softening of the emission at the pulse minima, due to the presence of a temperature gradient within the atmosphere (with the coolest layer at the surface). For many systems, however, only phase-integrated spectra are available due to inadequate photon statistics and/or time resolution. Such model X-ray spectra in which the geometry, strong gravity, and rotation of the NS have been taken into account are shown in Figure 2. It is apparent that in addition to a change in the total flux, there is a significant shift in the peak energy of the spectrum. For a BB spectrum no such variations are expected. Therefore, even in the case of phase-integrated spectra it is important to take into account the system geometry ( $\alpha$  and  $\zeta$ ) to ensure reliable measurements of the temperature and effective area of the hot spots.

### 3. APPLICATION

Close examination of equations (2) and (10) reveals that the flux observed at infinity from the hot spots depends on several important NS parameters. Figure 3 illustrates the effect of the stellar compactness on the pulse profile of a rotating NS with two antipodal hot spots covered with a H atmosphere. It is apparent that a small increase in  $M/R$  results in a substantial decrease in the pulsed fraction. This is a consequence of the strong sensitivity of light bending on the compactness of the star. Thus, as shown by Pavlov & Zavlin (1997) and Zavlin & Pavlov (1998), modeling of the spectra and pulse profile may, in principle, allow stringent constraints on  $M$  and  $R$ . Note that in the case of atmosphere models,

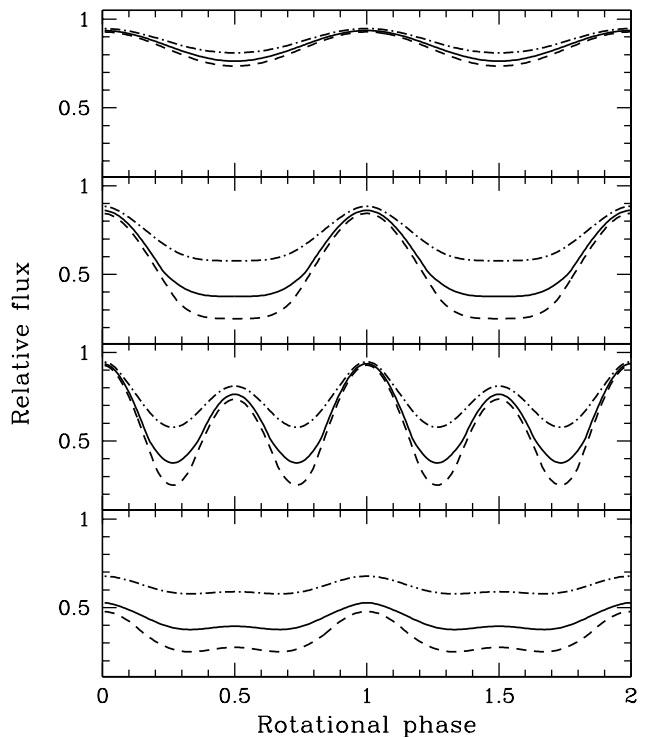


FIG. 3.— Model H atmosphere lightcurves for different stellar radii for an assumed  $1.4 M_{\odot}$  star. The curves correspond to  $R = 9$  km (*dot-dashed*), 12 km (*solid*), and 16 km (*dashed*). The values of  $\alpha$  and  $\zeta$  for each panel are the same as in Fig. 1. Two rotational cycles are shown for clarity.

$M$  and  $R$  also figure implicitly in the intensity  $I'(\nu', \theta')$  through the surface gravity  $g_s = (1 - R_S/R)^{-1/2} M/R^2$ . Although this dependence is much weaker than that through equation (2), it suggests that  $M$  and  $R$  should be treated as separate parameters. The spectra and lightcurves also depend strongly on the angles  $\alpha$  and  $\zeta$  through equations (1) and (2). In rotation-powered pulsars,  $\alpha$  corresponds to the pulsar obliquity, i.e. the angle between the spin and magnetic axes. Knowledge of this angle has important implications in the study of NS magnetic fields. Hence, an application of our model to X-ray spectroscopic and timing observations may yield useful constraints on  $M/R$ ,  $\alpha$ , and  $\zeta$ .

To allow direct comparison of our model with observational data we have generated a grid of H atmosphere emergent intensities,  $I'(\nu', \theta')$ , for a range of effective temperatures  $T_{\text{eff}}$ ,  $g_s$  (implying a range of  $M$  and  $R$ ), and  $\theta$ . This grid allows us to generate a spectrum and pulse profile for any desired values of  $M$ ,  $R$ ,  $\alpha$ , and  $\zeta$ . To minimize the number of free parameters, we fix  $M$  to  $1.4 M_{\odot}$  and vary only  $R$ . For the purposes of spectral analysis, we have incorporated our model into XSPEC<sup>3</sup> 12.3.0. The fits to the data are performed as in Pavlov & Zavlin (1997) and Zavlin & Pavlov (1998). We first fit the spectrum for assumed values of  $R$ ,  $\alpha$ , and  $\zeta$ . The resulting best fit  $T_{\text{eff}}$ ,  $R_{\text{eff}}$  (the effective radius of each hot spot), and  $N_{\text{H}}$  (the integrated H column density along the line of sight) are then used to generate the corresponding pulse profiles. After convolving with the appropriate detector response and accounting for background noise, the model lightcurves are binned to the same number of

<sup>3</sup> <http://heasarc.gsfc.nasa.gov/docs/xanadu/xspec/>

TABLE 1  
X-RAY OBSERVATIONS OF PSR J0437–4715

Observatory	Detector	Energy band (keV)	Exposure (ks)	Note <sup>a</sup>
<i>ROSAT</i>	PSPC	0.1–2	9.8	S+T
<i>Chandra</i>	ACIS-S	0.3–8	25.7	S
	HRC-S	0.1–10	19.6	T
<i>XMM-Newton</i>	EPIC-MOS	0.3–10	68.3	S
	EPIC-pn	0.3–10	67.2	S+T

REFERENCES. — Zavlin & Pavlov 1998; Zavlin et al. 2002; Zavlin 2006.

<sup>a</sup> S=spectroscopy, T=timing.

phase bins as the data, which allows a calculation of  $\chi^2$

$$\chi^2 = \sum_{i=1}^K \frac{(N_{o,i} - N_{m,i})^2}{N_{o,i} + N_{b,i}} \quad (11)$$

where  $N_{o,i}$ ,  $N_{m,i}$ , and  $N_{b,i}$  are the observed, model, and background counts in the  $i$ th phase bin, respectively, and  $K$  is the total number of bins. This procedure is repeated for a range of  $R$ ,  $\alpha$ ,  $\zeta$ , and  $N_H$  to map the multidimensional  $\chi^2$  surface and derive confidence levels for these parameters.

### 3.1. The Radio Millisecond Pulsar PSR J0437–4715

Recent X-ray observations have revealed that the emission from most rotation-powered MSPs (Becker & Achenbach 2002; Grindlay et al. 2002; Zavlin 2006; Bogdanov et al. 2006a) is of predominantly thermal nature. This radiation is believed to originate from the magnetic polar caps of the pulsar that are heated by a back-flow of high-energy particles from the magnetosphere (see e.g., Harding & Muslimov 2002). Given that the progenitors of radio MSPs undergo an extended period of accretion during the low-mass X-ray binary phase (Alpar et al. 1982; Bhattacharya & van den Heuvel 1991) it is reasonable to expect these stars to have accumulated a substantial surface layer of gas. Due to the immense surface gravity the accreted material quickly stratifies, with the lightest element remaining on top and dominating the observed emission. Therefore, the existence of a thick light element atmosphere at the surface of MSPs is highly likely (Zavlin et al. 1995a). Note that for the quality of the available spectral data of MSPs, at the temperatures relevant for these sources a He atmosphere is virtually indistinguishable from a H one, although based on the standard formation scenario of MSPs the existence of H at the surface is more probable. Also, Rajagopal & Romani (1996) and Zavlin et al. (2002) have shown that a heavy element (Fe) atmosphere does not provide a good description of MSP spectra.

Of the  $\sim 40$  X-ray detected radio MSPs, at present, only PSR J0437–4715 (Johnston et al. 1993), the nearest and brightest, has X-ray data of sufficient quality to permit detailed modeling of its spectrum and pulse profile. Zavlin et al. (2002) and Zavlin (2006) have shown that the spectrum of this pulsar is well described by a multi-component model consisting of two dominant hydrogen atmosphere thermal components with temperatures  $T_1 = (2.1 - 1.5) \times 10^6$  K and  $T_2 = (0.52 - 0.54) \times 10^6$  K and effective radii  $R_1 \approx 0.34$  km and  $R_2 \approx 2.0$  km, for

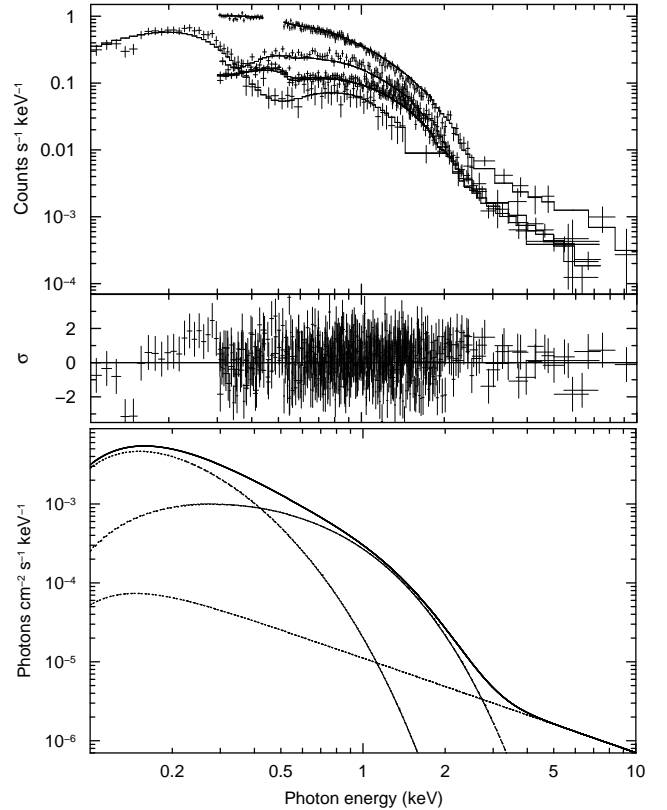


FIG. 4.— (Upper panels) *ROSAT* PSPC, *Chandra* ACIS-S, and *XMM-Newton* EPIC-MOS1/2 and EPIC-pn spectra of PSR J0437–4715. The lines show a representative best fit of our model to the data. The bottom panel shows the best fit residuals. (Lower panel) Representative best-fit model spectrum consisting of two hydrogen atmosphere and one PL components.

assumed  $M = 1.4 M_\odot$ ,  $R = 10$  km,  $\alpha = 45^\circ$  and  $\zeta = 45^\circ$ . The presence of two temperatures can be attributed to non-uniform heating of the polar caps by the return flow of magnetospheric particles (see Harding & Muslimov 2002; Zhang & Cheng 2003).

A faint power-law (PL) tail is also observed from this MSP at energies  $\gtrsim 2$  keV. The nature of this PL emission is ambiguous as it may arise either due to magnetospheric emission processes or weak Comptonization of the thermal radiation by the tenuous magnetospheric plasma (Bogdanov et al. 2006b). A crucial difference between the two interpretations is that in the former the PL component extends to energies well below the soft X-ray band, while in the latter the PL is only present at higher energies ( $\gtrsim 2$  keV). Moreover, the magnetospheric emission PL is inconsistent with the FUV flux from this MSP (Kargaltsev et al. 2004) unless its spectral photon index is  $\Gamma \lesssim 1.6$ .

Previously, Pavlov & Zavlin (1997) and Zavlin & Pavlov (1998) have applied a two-temperature hydrogen atmosphere polar cap model to spectroscopic and timing *ROSAT* PSPC observations of PSR J0437–4715 in an effort to constrain  $M/R$  of this NS. In this analysis, a centered dipole field was considered. Based on this assumption a limit of  $R > 8.8$  km for  $M = 1.4 M_\odot$  was obtained. As deeper observations of this MSP have become available since, it is worth revisiting this object to determine if better constraints on  $M/R$  can be

obtained.

We have retrieved archival *ROSAT*, *Chandra*, and *XMM-Newton* spectral and timing observations of this MSP to investigate its X-ray emission. These observations are summarized in Table 1. It is important to note that the values for the effective temperatures and radii derived by Zavlin et al. (2002) and Zavlin (2006) are by no means unique as they are sensitive to the initial choice of  $M$ ,  $R$ , and (as evident in Fig. 2)  $\alpha$  and  $\zeta$ . We have carried out a series of spectral fits for  $M = 1.4$ ,  $R = 8 - 16$  km,  $\alpha = 0^\circ - 90^\circ$ ,  $\zeta = 0^\circ - 90^\circ$ <sup>4</sup>, and  $N_{\text{H}} = (1 - 3) \times 10^{19}$  cm<sup>-2</sup>. For this set of parameters, we find  $T_1 = 1.43 - 1.85$  MK,  $R_1 = 0.04 - 0.40$  km,  $T_2 = 0.4 - 0.56$  MK, and  $R_2 = 1.8 - 4.9$  km, with  $\chi_\nu^2 = 1.3$  for 402 degrees of freedom. The ranges quoted give the  $\pm 1\sigma$  bounds for one interesting parameter. Given the known cross-calibration uncertainties of the various detectors, the minimum value of  $\chi_\nu^2$  corresponds to an acceptable fit and indicates a systematic uncertainty at the level of  $\sim 5-10\%$ . These results are generally in good agreement with those derived in previous studies. We have performed the spectral fits for two cases: PL emission with  $\Gamma \lesssim 1.6$  and no PL emission below 2 keV as an approximation to a Comptonization model. In both cases, we find that such a component contributes with  $\lesssim 5\%$  to the total photon flux below 2 keV. Furthermore, although the statistics at high energies are quite limited, *XMM-Newton* EPIC-pn data above 3 keV suggest that the PL does not show sharp pulsations (cf Fig. 3 of Bogdanov et al. 2006b) as observed in the more luminous MSPs, PSRs B1937+21 (Nicastro et al. 2004) and B1821-24 (Rutledge et al. 2004). This implies that the observed pulse shape is not significantly affected by the PL emission. Therefore, in our lightcurve analysis we will include this component as a constant (DC) contribution to the pulsed flux.

### 3.2. Fits to the Pulse Profile of PSR J0437-4715

Using the derived range of temperatures and radii we proceed to generate synthetic pulse profiles and compare them to those of J0437-4715. When folded at the spin period ( $P = 5.76$  ms), the X-ray emission from this MSP exhibits a single broad pulse, with pulsed fraction 30-40%, depending on the choice of energy band (see Zavlin 2006), consistent with thermal radiation. A visual comparison with the lightcurves in Figure 1 shows that the X-ray pulsations of this MSP (Fig. 5) most closely resemble those of classes I and II. However, it is immediately apparent that the pulses of J0437-4715 are asymmetric, characterized by a faster decrease than increase in flux. This is clearly inconsistent with the antipodal hot spot model. In addition, at the spin period of this MSP the Doppler effect is fairly weak so it cannot reproduce the degree of asymmetry observed. Indeed, an acceptable fit could not be obtained for any combination of  $R$ ,  $\alpha$ , and  $\zeta$ . The discrepancy can be resolved if the two hot spots are not diametrically opposite, i.e. if the magnetic axis is off-center. Therefore, in our model we introduce two additional free parameters,  $\Delta\phi$  and  $\Delta\alpha$ , offsets in  $\phi$  and

<sup>4</sup> For either  $\alpha$  or  $\zeta$ , the range  $90^\circ - 180^\circ$  becomes equivalent to  $90^\circ - 0^\circ$  if we reassign the secondary hot spot to be the primary and apply the transformation  $\phi \rightarrow \phi + \pi$ . Therefore, it is only necessary to consider the latter range.

$\alpha$ , respectively, of the secondary hot spot. These correspond to displacements on the NS surface in longitude and latitude, respectively, from the antipodal position. The net offset on the stellar surface of the secondary hot spot from the antipodal position is

$$\Delta s = R \cos^{-1}[-\sin \alpha \sin(\alpha + \Delta\alpha) - \cos \alpha \cos(\alpha + \Delta\alpha) \cos \Delta\phi] \quad (12)$$

In an offset dipole configuration  $\alpha$  is no longer the angle between the spin and magnetic axes and the dipole axis does not run through the center of the star. The total displacement (i.e. impact parameter) of the magnetic axis from the center is then

$$\Delta x = R \sin\left(\frac{\Delta s}{2R}\right) \quad (13)$$

If we introduce an offset dipole, we find that a phase lag of  $\Delta\phi \sim -20^\circ$ , implying  $\Delta x \sim 1$  km, is able to account for the asymmetry in the pulse profile.

In the formal fits to the X-ray pulse profiles of PSR J0437-4715 we consider nine free parameters:  $T_1$ ,  $R_1$ ,  $T_2$ ,  $R_2$ ,  $R$ ,  $\alpha$ ,  $\zeta$ ,  $\Delta\alpha$ , and  $\Delta\phi$ , while keeping  $N_{\text{H}}$  fixed at  $2 \times 10^{19}$  cm<sup>-2</sup> and  $M$  at  $1.4 M_\odot$ . In addition, since the relative phase between the various observations cannot be determined due to the inadequate absolute timing precision of *ROSAT* and *XMM-Newton*, we allow the  $\phi$  to vary independently for each dataset. The model was fitted individually to *ROSAT* PSPC (0.1-2.4 keV), *Chandra* HRC-S (0.1-10 keV), and *XMM-Newton* (0.3-2 keV) timing data. For the latter, the availability of spectral information and the sufficient photon statistics permit us to consider two energy bands: 0.3-0.7<sup>5</sup> and 0.7-2 keV, where the cool and hot thermal component dominate, respectively. Since the effects of the system geometry and strong gravity are purely achromatic, the availability of multiple energy bands is very useful as it enables a test of the validity of the atmosphere model, which exhibits characteristic energy dependent effects (as described in §2.2). Due to the 10-fold better photon statistics of the *XMM-Newton* dataset, compared to the *ROSAT* PSPC and *Chandra* HRC-S data, it provides the best constraints on the desired parameters. We have considered the other data, nonetheless, as they provide a useful consistency check of the model. The best-fit parameters and confidence intervals were determined by manually searching the  $\chi^2$  hyperspace for the minimum. In principle, an additional strong constraint can be imposed by requiring that the derived temperatures and radii from these fits be within  $3\sigma$  of those obtained from the spectral analysis. Unfortunately, due to the limited photon statistics as well as the relatively large cross-calibration uncertainties of the detectors, which are clearly evident in Figure 4, the  $3\sigma$  range of derived temperatures ( $T_1 = 1.35 - 1.95$  MK and  $T_2 = 0.39 - 0.60$  MK) is not particularly constraining.

The atmosphere model is able to reproduce the shape of the pulse profile and variation in pulsed fraction with energy remarkably well, as is evident in Figures 5 and 6. As a consequence of the numerous free parameters and the complex covariances that exist between them, ac-

<sup>5</sup> For this energy range, the 0.44-0.51 keV band was excluded to eliminate an instrumental feature specific to the fast timing mode of the EPIC-pn detector.

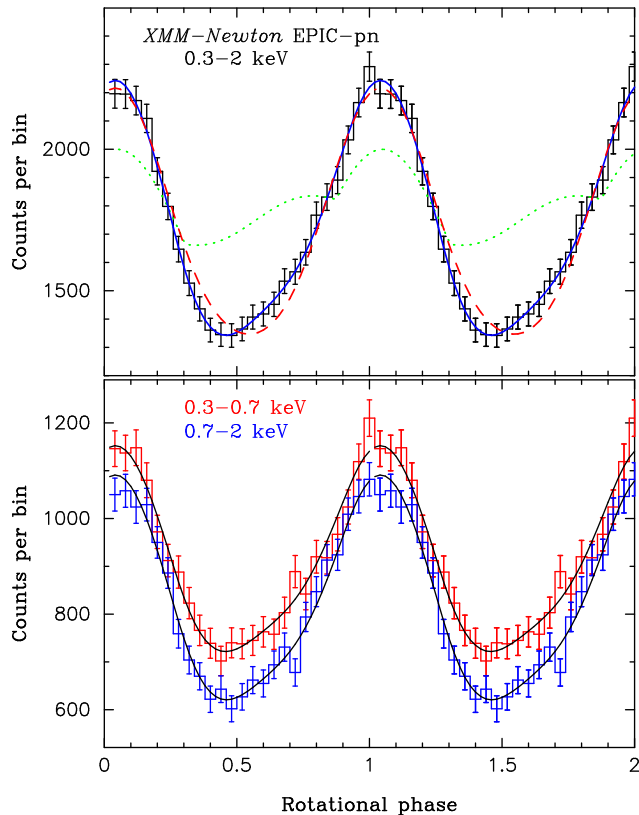


FIG. 5.— (Top) *XMM-Newton* EPIC-pn 0.3–2 keV pulse profile of PSR J0437–4715. The solid line shows the best fit curve for an off-center dipole field and a H atmosphere with  $R = 9.6$  km,  $\alpha = 30^\circ$ ,  $\zeta = 42^\circ$ ,  $\Delta\alpha = -12^\circ$ ,  $\Delta\phi = -20^\circ$ ,  $T_1 = 2.02$  MK,  $R_1 = 0.2$  km,  $T_2 = 0.48$  MK,  $R_2 = 3.5$  km, and  $N_H = 2 \times 10^{19}$  cm $^{-2}$ . The dotted line is of a blackbody that best fits the spectrum of J0437–4715 for the same assumed compactness and geometry. The dashed line corresponds to the best fit H atmosphere model for a centered dipole. (Bottom) Best fits to the *XMM-Newton* EPIC-pn pulse profiles in the 0.3–0.7 keV and 0.7–2 keV bands (upper and lower curve, respectively) assuming an off-center dipole. The choice of phase 0 is arbitrary.

ceptable values of  $\chi^2$  were obtained for a relatively wide range of parameter values. Fortunately, the strong correlations can be weakened if we fix the angle  $\zeta$  to its most likely value. Radio timing observations indicate that the orbital inclination of the J0437–4715 binary system is  $i = 42^\circ$  (van Straten et al. 2001; Hotan et al. 2006). It is highly probable that the spin axis of the MSP is closely aligned with the orbital angular momentum vector as a direct result of the spin-up process during the LMXB phase. If this is indeed the case, the angle between the spin axis and the line of sight must be  $\zeta \approx 42^\circ$ . This constraint significantly constricts the allowed parameter space and thus improves the accuracy with which the other parameters can be determined. In particular, for the fit to the *XMM-Newton* EPIC-pn pulse profiles we find the  $\pm 1\sigma$  ranges to be:  $R = 6.9 - 10.6$  km,  $\alpha = 25^\circ - 90^\circ$ ,  $\Delta\alpha = -50^\circ - 20^\circ$ ,  $\Delta\phi = -(23^\circ - 14^\circ)$ ,  $T_1 = 1.4 - 1.85$  MK,  $T_2 = 0.4 - 0.54$  MK,  $R_1 = 0.1 - 0.36$  km, and  $R_2 = 2.0 - 3.5$  km. All ranges quoted represent  $1\sigma$  confidence intervals. Varying  $N_H$  over the range  $(1 - 3) \times 10^{19}$  cm $^{-2}$  does not cause significant changes in the derived results since the interstellar extinction towards this MSP is negligible above  $\sim 0.3$  keV. The de-

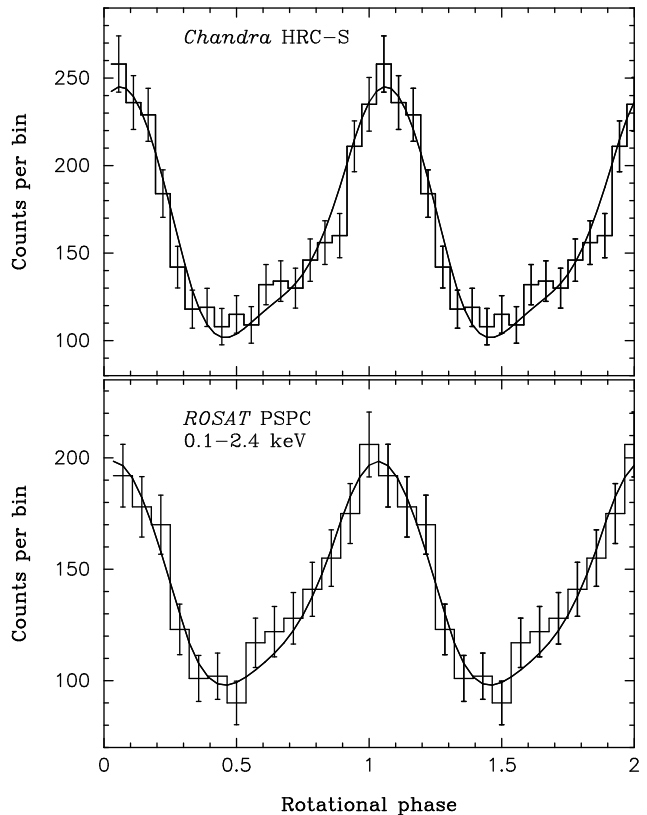


FIG. 6.— *Chandra* HRC-S (top), and *ROSAT* PSPC (bottom) pulse profiles of J0437–4715. The solid lines show the best fit model to the *XMM-Newton* EPIC-pn data. The flux normalization  $R_{\text{eff}}^2/D^2$  has been adjusted to correct for the discrepancies in the absolute calibration of the different detectors (see text for details).

rived values of  $\Delta\phi$  and  $\Delta\alpha$  translate into an offset of the magnetic axis from the center of the star of  $\Delta x = 0.8 - 3$  km ( $1\sigma$ ). For  $R$  we are also able to derive 90% and 99.9% limits of 6.8 – 13.9 km and  $>6.7$  km, respectively (see Fig. 7); similar limits are obtained even without the constraint on  $\zeta$ . The fits to the *ROSAT* PSPC and *Chandra* HRC-S pulse profiles are generally consistent with these results if we account for the systematic uncertainties encountered in the spectral fits. We note in passing that the best fit parameters for PSR J0437–4715 derived by Zavlin & Pavlov (1998) using the *ROSAT* PSPC as well as their assumption of a centered dipole do not yield acceptable fits to the *Chandra* HRC-S and *XMM-Newton* EPIC-pn pulse profiles, even if we account for cross-calibration uncertainties.

We have found that  $\alpha$  and  $\Delta\alpha$  are the two parameters that are most strongly covariant with  $R$  (see Fig. 8).  $\Delta\alpha$ , in particular, closely mimics the effects of  $M/R$  on the observed pulse profiles (Fig. 3), thus weakening the constraint on  $R$ . If  $\alpha$  and  $\Delta\alpha$  for this MSP can be determined by independent means (e.g., from radio polarization measurements), the accuracy of the measurement of  $R$  can be greatly improved.

We have conducted the entire fitting procedure outlined above for a BB emission model as well. We find that the thermal portion of the X-ray spectrum is well described by a two-temperature BB model. This is expected, given the close qualitative similarities between the BB and H atmosphere spectra. However, a BB

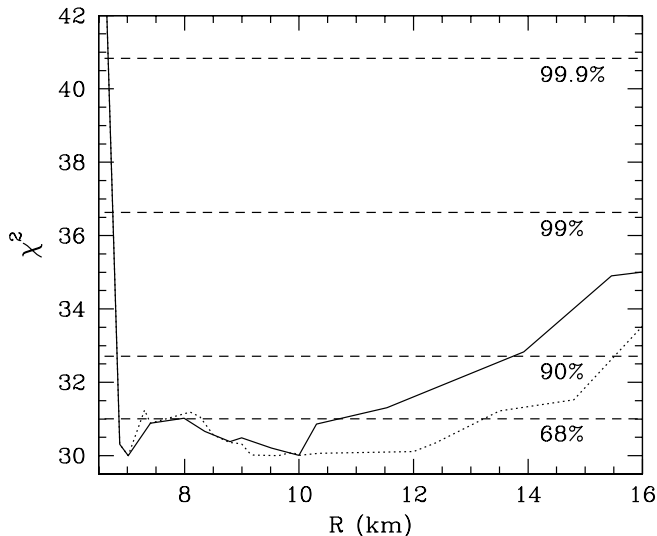


FIG. 7.— The effect of the stellar radius on the  $\chi^2$  statistic of the fit to the *XMM-Newton* EPIC-pn pulse profile of PSR J0437–4715 for  $M = 1.4 M_{\odot}$ . The solid line corresponds to a fixed value of  $\zeta = 42^\circ$ , while the dotted line is for no constraint on  $\zeta$ . The dashed lines show the 68%, 90%, 99%, and 99.9% confidence levels for one interesting parameter.

model is incapable of reproducing the pulse shape and pulsed fraction for any  $R$ . Furthermore, a BB cannot account for the observed changes in the pulsed fraction as a function of photon energy (see Fig. 5). Therefore, we confirm the finding of Pavlov & Zavlin (1997) and Zavlin & Pavlov (1998) that *a blackbody is not a valid description of the surface of J0437–4715, implying that an optically thick, light-element atmosphere must be present on the stellar surface.*

#### 4. DISCUSSION

The principal motivation of our analysis is to extract information regarding the compactness of the NS, magnetic field configuration, and radiative properties of the stellar surface. It is important to realize, however, that the method of inferring these properties is inherently model dependent. Thus, it is necessary to examine the validity of the approximations and assumptions we have made as well as any potential bias that they may introduce in the derived results. This is especially critical for determination of  $M/R$  if this approach is to be used to place stringent constraints on the NS equation of state (EOS).

One of the underlying assumptions of the atmosphere model is that the source of heat is below the atmospheric layer. At first, this seems to be at odds with the prediction of pulsar electrodynamic models that the MSP polar caps are heated by a return current of ultra-relativistic electrons/positrons from the magnetosphere above the polar caps. However, the penetration depth of the impinging particles is significantly larger than the characteristic depth of the hydrogen atmosphere. In particular, the stopping column of a relativistic electron in hydrogen, assuming energy loss via bremsstrahlung and a negligible magnetic field, is  $y \sim 60 \text{ g cm}^{-2}$  (Tsai 1974, and references therein). For comparison, in the case of a hydrogen atmosphere with  $\log T_{\text{eff}} \sim 5.6\text{--}6.4$  the characteristic depth is  $\sim 0.01\text{--}1 \text{ g cm}^{-2}$  (cf Fig. 2 of Zavlin et al.

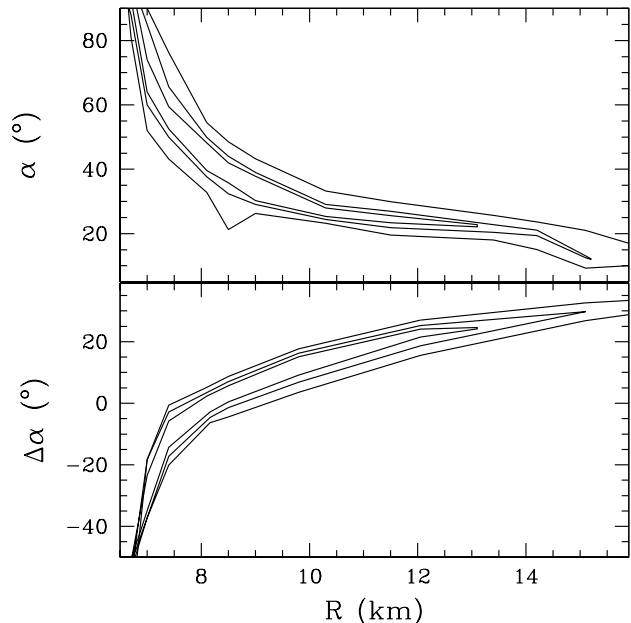


FIG. 8.— 68%, 90%, and 99.9% confidence contour plots showing the correlation between the stellar radius  $R$  and  $\alpha$  (top) and  $\Delta\alpha$  (bottom) for  $M = 1.4 M_{\odot}$  in the fit to the *XMM-Newton* EPIC-pn pulse profile of PSR J0437–4715.

1996). Therefore, the bulk of the energy of the returning particles is deposited well below the depth at which the atmosphere becomes optically thick.

For PSR J0437–4715, the relatively long spin period ( $P = 5.76 \text{ ms}$ ) suggest that the rapid rotation has a negligible effect on the shape of the star. Hence, our assumption of spherical Schwarzschild geometry is appropriate. Also, based on the pulsar period ( $P = 5.76 \text{ ms}$ ) and acceleration-corrected period derivative ( $1.86 \times 10^{-20} \text{ s}^{-1}$ ) we find that the magnetic field strength at the surface of the MSP polar caps is  $B_{\text{surf}} \propto (P\dot{P})^{1/2} \approx 3.3 \times 10^8 \text{ G}$  so the assumption of an unmagnetized atmosphere is correct (Zavlin et al. 1995a).

In our analysis of PSR J0437–4715 we have ignored any thermal emission outside of the polar cap regions. *Hubble Space Telescope* FUV observations of this MSP (Kargaltsev et al. 2004) indicate that the rest of the star is at a temperature  $T_{\text{eff}} \sim 10^5 \text{ K}$ . Given that this emission peaks in the UV, its contribution to the X-ray flux is insignificant.

Another simplifying assumption we have introduced is that of point-like emission regions. To determine the effect of this approximation, we have compared model pulse profiles of point-like and extended circular emission areas with  $R_{\text{eff}} \sim 2\text{--}4 \text{ km}$ , comparable to those inferred for the cooler emission component of the spectrum of PSR J0437–4715. We find that the maximum difference between the two cases, occurring at  $\phi \approx 0$  and  $\phi \approx 0.5$ , is only  $\sim 1\%$ , which is significantly lower than the statistical uncertainty of the presently available timing data. Therefore, the hot spots are truly point-like so this approximation is more than adequate. Note that for X-ray timing data with better photon statistics, the exact size and shape of the emission regions may become important and may, in principle, be measurable quanti-



ties.

We have also assumed that the two thermal components occupy the same  $(\phi, \alpha)$  location on the NS surface. The lack of any appreciable phase shift between the cool (0.3–0.7 keV) and hot (0.7–2 keV) components, as determined from the highest quality (*XMM-Newton* EPIC-pn) data, implies that the two emission regions are effectively concentric. The detection of any such phase difference would provide interesting information regarding the temperature distribution across the polar caps.

It is important to emphasize that the possible presence of faint PL emission below  $\sim 2$  keV in the spectrum of PSR J0437–4715 does not prohibit reliable constraints on the properties of the underlying NS. This component only introduces a small increase in the uncertainty of our measurement. With future deep phase-resolved spectroscopic observations the true nature of the PL can be determined and the temporal properties of this component can be properly modeled, resulting in improved constraints on the desired NS properties.

Along with insufficient photon statistics, one of the main factors limiting the accuracy of our measurement of  $M/R$  is the uncertainty in the calibration of the X-ray detectors used in this analysis. As noted in §3, this problem precludes a precise determination of  $T_1$  and  $T_2$  from the spectral fits, which can provide much tighter constraints on  $M/R$  than obtained in our analysis. Note that the uncertainty in detector performance has lesser impact on the fits to the pulse profiles, which are integrated over a relatively wide energy band so that deviations in the spectral response tend to average out. Moreover, this uncertainty mostly effects the flux normalization  $R_{\text{eff}}^2/D^2$  of the pulse profile and has little bearing on the validity of our measurement of  $R$  and the conclusions regarding the presence of an atmosphere on the NS surface and magnetic field geometry. Improvement in the detector calibration will enable much tighter constraints on  $M/R$ .

## 5. CONCLUSIONS

We have presented a model of thermal emission from rotating NSs covered with an unmagnetized hydrogen atmosphere, applicable to systems for which the radiation is localized in small regions on the surface. Such a configuration is expected in MSPs. Indeed, the model lightcurves (Figs. 1 and 3) are qualitatively similar to the observed thermal pulse profiles of nearby MSPs in the field of the Galaxy (Becker & Achenbach 2002; Zavlin 2006). In addition, the broad modulations and moderate pulsed fractions ( $\lesssim 50\%$ ) of the lightcurves produced by our model are in full agreement with the limits obtained for the thermal MSPs in 47 Tuc (Cameron et al. 2007).

An application to the nearest radio MSP J0437–4715 shows that the spectral and temporal properties of its X-ray emission are easily reproduced by our model, without the need to resort to contrived assumptions regarding the properties of the NS atmosphere (composition and thickness, see, e.g., Ho et al. 2007; Mori & Ho 2007) and the temperature distribution across the stellar surface. This excellent agreement allows valuable insight into important NS properties that are not measurable by other means. Specifically, we confirm that the radiative properties of the NS surface are fully consistent with a light

element atmosphere model and are poorly reproduced by a blackbody. This provides compelling evidence that the surface of this MSP is indeed covered by a gaseous layer of hydrogen. Note that this result does not necessarily apply to all varieties of NS systems given that MSPs are formed via a special evolutionary channel, involving prolonged accretion of gas from a close stellar companion. The pulse profile of J0437–4715 suggests that the global magnetic field configuration closely resembles a dipole, albeit one significantly offset from the stellar center. It is unclear whether this displacement is primordial, i.e., the result of the core-collapse that formed the NS, the result of magnetic field burial during the LMXB phase or a consequence of magnetic field evolution and migration as proposed by Ruderman (1991). We note that small scale deviations from a pure dipole, with characteristic scales  $\ll R$ , may still exist near the NS surface. Ultra-deep X-ray spectroscopic and timing observations may, in principle, reveal such “microstructure”, which could be manifested in the form of temperature variations across the face of the polar caps.

Perhaps the most important practical application of our model is a constraint on the compactness of the NS, which has important implications for determination of the true NS EOS. In particular, the restriction of  $R > 6.7$  km (at 99.9% confidence) for a  $M = 1.4 M_{\odot}$  star implies that PSR J0437–4715 is not ultra-compact, i.e. not smaller than its photon sphere. For this and other binary MSPs a very accurate, independent measurement of the NS mass is possible using radio timing observations. Thus, in principle, a unique determination of the stellar radius can be achieved. Note that for J0437–4715, the two mass measurements of  $M = 1.58 \pm 0.18$  (van Straten et al. 2001) and  $M = 1.3 \pm 0.2 M_{\odot}$  (Hotan et al. 2006) currently available do not provide very tight constraints on the allowed masses.

Despite the inherent model dependence of this approach and the relatively large number of free parameters we are able to extract valuable information regarding the poorly understood properties of pulsars and neutron stars, in general. Moreover, as discussed in §4, the conclusions drawn from our analysis are fairly robust in the sense that they are weakly sensitive to the underlying assumptions and approximations. Future deep observations of PSR J0437–4715 and other MSPs can provide even more stringent constraints on fundamental NS parameters. One close MSP ( $D \approx 300$  pc), PSR J0030+0451 (Becker & Achenbach 2002; Lommen et al. 2006), exhibits a double peaked X-ray pulse profile, indicating a viewing angle and pulsar obliquity substantially different from those of J0437–4715. As such, this pulsar is ideal for an independent verification of this method. An upcoming deep *XMM-Newton* observation will allow a detailed study of PSR J0030+0451.

MSPs are much better suited for this analysis than other NS systems such as X-ray binaries, isolated NSs, and normal pulsars. In the latter objects there are numerous complications arising due to the effects of the strong magnetic field on the emergent thermal radiation, the unknown temperature distribution across the surface, severe reprocessing of the thermal radiation by the magnetosphere, and the uncertain emission altitude above the NS surface (e.g. in X-ray bursts, Cottam et al. 2006). Their low magnetic fields, point-like emission

regions, and non-variable, dominant thermal emission make MSPs suitable laboratories for tests of fundamental NS physics and constraints on their EOS.

We would like to thank Ramesh Narayan and Bryan Gaensler for numerous insightful discussions. We also

thank the anonymous referee for many useful comments that helped improve the manuscript. This work was supported in part by NASA grant AR6-7010X. The research presented here has made use of the NASA Astrophysics Data System (ADS).

## REFERENCES

- Alpar, M. A., Cheng, A. F., Ruderman, M. A., & Shaham, J. 1982, *Nature*, 300, 728
- Becker, W. & Achenbach, B. 2002, *Proceedings of the 270. WE-Heraeus Seminar on Neutron Stars, Pulsars, and Supernova Remnants*, ed. W. Becker, H. Lech, & J. Trümper, p.64
- Beloborodov, A. M. 2002, *ApJ*, 566, L85
- Bhattacharya, D. & van den Heuvel, E. P. J. 1991, *Phys. Rep.*, 203, 1
- Bogdanov, S., Grindlay, J. E., Heinke, C. O., Camilo, F., Freire, P. C. C., & Becker, W. 2006a, *ApJ*, 646, 1104
- Bogdanov, S., Grindlay, J. E., & Rybicki, G. B. 2006b, *ApJ*, 648, L55
- Braje, T. M., Romani, R. W., & Rauch, K. P. 2000, *ApJ*, 531, 447
- Cadeau, C., Morsink, S. M., Leahy, D., & Campbell, S. S. 2007, *ApJ*, 654, 458
- Cameron, P. B., Rutledge, R. E., Camilo, F., Bildsten, L., Ransom, S. M., & Kulkarni, S. R. 2007, *ApJ*, in press
- Chatterjee, S., Gaensler, B. M., Melatos, A., Brisken, W. F., & Stappers, B. W. 2007, *ApJ*, in press (astro-ph/0703181)
- Cottam, J., Paerels, F., & Mendez, M. 2006, *Nature*, 420, 51
- Ftaclas, C., Kearney, M. W., & Pechenick, K. 1986, *ApJ*, 300, 203
- Grindlay, J. E., Camilo, F., Heinke, C. O., Edmonds, P. D., Cohn, H., & Lugger, P. 2002, *ApJ*, 581, 470
- Harding, A. K. & Muslimov, A. G. 2002, *ApJ*, 568, 862
- Heinke, C. O., Rybicki, G. B., Narayan, R., & Grindlay, J. E. 2006, *ApJ*, 644, 1090
- Ho, W. C. G., Kaplan, D. L., Chang, P., van Adelsberg, M., & Potekhin, A. Y. 2007, *MNRAS*, 375, 821
- Hotan, A. W., Bailes, M., & Ord, S. M. 2006, *MNRAS*, 369, 1502
- Johnston, S., Lorimer, D. R., Harrison, P. A., Bailes, M., Lyne, A. G., Bell, J. F., Kaspi, V. M., Manchester, R. N., D'Amico, N., & Nicastro, L. 1993, *Nature*, 361, 613
- Kargaltsev, O. Y., Pavlov, G. G., & Romani, R. W. 2004, *ApJ*, 602, 327
- Lattimer, J. M. & Prakash, M. 2001, *ApJ*, 550, 426
- Lommen, A. N., Kipphorn, R. A., Nice, D. J., Splaver, E. M., Stairs, I. H., & Backer, D. C. 2006, *ApJ*, 642, 1012
- McClintock, J. E., Narayan, R., & Rybicki, G. B. 2004, *ApJ*, 615, 402
- Miller, M. C. & Lamb, F. K. 1998, *ApJ*, 499, L37
- Misner, C. W., Thorne, K. S., & Wheeler, J. A. 1970, *Gravitation* (New York: Freeman)
- Mori, K. & Ho, W. C. G. 2007, *MNRAS*, 377, 905
- Nicastro, L., Cusumano, G., Löhmer, O., Kramer, M., Kuiper, L., Hermsen, W., Mineo, T., & Becker, W. 2004, *A&A*, 413, 1065
- Page, D. 1998, *The Many Faces of Neutron Stars*, ed. R. Buccheri, J. van Paradijs, M. A. Alpar, p. 539
- Pavlov, G. G. & Zavlin, V. E. 1997, *ApJ*, 490, L91
- Pechenick, K. R., Ftaclas, C., & Cohen, J. M. 1983, *ApJ*, 274, 846
- Poutanen, J. & Gierliński, M. 2003, *MNRAS*, 343, 1301
- Rajagopal, M. & Romani, R. W. 1996, *ApJ*, 461, 327
- Riffert, H. & Mészáros, P. 1988, *ApJ*, 325, 207
- Romani, R. W. 1987, *ApJ*, 313, 718
- Ruderman, M. 1991, *ApJ*, 366, 261
- Rutledge, R. E., Fox, D. W., Kulkarni, S. R., Jacoby, B. A., Cognard, I., Backer, D. C., & Murray, S. S. 2004, *ApJ*, 613, 522
- Shibanov, Iu. A., Zavlin, V. E., Pavlov, G. G., & Ventura, J. 1992, *A&A*, 266, 313
- Tsai, Y.-S. 1974, *Rev. Mod. Phys.*, 46, 815
- van Straten, W., Bailes, M., Britton, M., Kulkarni, S. R., Anderson, S. B., Manchester, R. N., & Sarkissian, J. 2001, *Nature*, 412, 158
- Viiroinen, K. & Poutanen, J. 2004, *A&A*, 426, 985
- Zane, S. & Turolla, R. 2006, *MNRAS*, 366, 727
- Zavlin, V. E., Shibanov, Y. A., & Pavlov, G. G. 1995a, *Astron. Lett.*, 21, 149
- Zavlin, V. E., Pavlov, G. G., Shibanov, Y. A., & Ventura, J. 1995b, *A&A*, 297, 441
- Zavlin, V. E., Pavlov, G. G., & Shibanov, Yu. A., 1996, *A&A*, 315, 141
- Zavlin, V. E. & Pavlov, G. G. 1998, *A&A*, 329, 583
- Zavlin, V. E., Pavlov, G. G., Sanwal, D., Manchester, R. N., Trümper, J., Halpern, J. P., & Becker, W. 2002, *ApJ*, 569, 894
- Zavlin, V. E. 2006, *ApJ*, 638, 951
- Zhang, L. & Cheng, K. S. 2003, *A&A*, 398, 639